PHYSICS

Spontaneous phase segregation of Sr_2NiO_3 and $SrNi_2O_3$ during $SrNiO_3$ heteroepitaxy

Le Wang[1]*, Zhenzhong Yang[1]*†, Xinmao Yin[2]*, Sandra D. Taylor[1], Xu He[3], Chi Sin Tang[4], Mark E. Bowden[5], Jiali Zhao[6], Jiaou Wang[6], Jishan Liu[1,7], Daniel E. Perea[8], Linda Wangoh[1], Andrew T. S. Wee[2], Hua Zhou[9], Scott A. Chambers[1]‡, Yingge Du[1]‡

Recent discovery of superconductivity in $Nd_{0.8}Sr_{0.2}NiO_2$ motivates the synthesis of other nickelates for providing insights into the origin of high-temperature superconductivity. However, the synthesis of stoichiometric $R_{1−x}Sr_xNiO_3$ thin films over a range of x has proven challenging. Moreover, little is known about the structures and properties of the end member $SrNiO_3$. Here, we show that spontaneous phase segregation occurs while depositing $SrNiO_3$ thin films on perovskite oxide substrates by molecular beam epitaxy. Two coexisting oxygen-deficient Ruddlesden-Popper phases, Sr_2NiO_3 and $SrNi_2O_3$, are formed to balance the stoichiometry and stabilize the energetically preferred Ni^{2+} cation. Our study sheds light on an unusual oxide thin-film nucleation process driven by the instability in perovskite structured $SrNiO_3$ and the tendency of transition metal cations to form their most stable valence (i.e., Ni^{2+} in this case). The resulting metastable reduced Ruddlesden-Popper structures offer a testbed for further studying emerging phenomena in nickel-based oxides.

INTRODUCTION

Rare-earth nickelates ($RNiO_3$, where R denotes the lanthanide) exhibit a rich array of structural and physical properties (1–3). Although bulk $LaNiO_3$ (LNO) is a rhombohedral structured paramagnetic metal at all temperatures, other $RNiO_3$ compounds display metal-to-insulator transitions (MITs) from a high-temperature orthorhombic metallic phase to a low-temperature monoclinic insulating phase. The orthorhombic structure (Fig. 1A) evolves from a distortion of the cubic structure due to a small Goldschmidt tolerance factor (t). The drop in t with decreasing R cation radius tends to drive the distortion and reduce the Ni—O—Ni bond angle, resulting in a reduction in Ni $3d$–O $2p$ orbital overlap. Consequently, the bandwidth drops and the transition temperature goes up.

Doping and strain engineering are two common ways to modify the electronic states of $RNiO_3$ for exploring emergent physical properties and potential applications (4–10). The recent discovery of superconductivity in infinite-layered $Nd_{0.8}Sr_{0.2}NiO_2$ on $SrTiO_3$ substrates motivates the synthesis of other related nickelates in searching for high T_c materials and exploring the origin of the observed superconductivity (11). However, insulating behavior without the presence of superconductivity was observed in bulk $Nd_{0.8}Sr_{0.2}NiO_2$ samples (12, 13), suggesting that superconductivity in this system may arise from interface or strain-related effects. Hence, the synthesis of high-quality stoichiometric $Nd_{1−x}Sr_xNiO_3$ thin films with controlled x becomes a prerequisite for further harnessing superconductivity in this system. However, the synthesis of stoichiometric $R_{1−x}Sr_xNiO_3$ thin films over a wide range of x has proven to be difficult (10, 11, 14) because of the instability of Ni oxidation states greater than +3. It is thus of considerable interest to explore how the structure and properties of nickelate thin films evolve at higher x, why structural decay occurs as x increases, and whether the end member $SrNiO_3$ can be stabilized as a (pseudo)cubic perovskite by epitaxial growth. In addition, a Ruddlesden-Popper (RP)–type secondary phase is often observed during the growth of nickelate thin films (14). However, it is not clear why the RP secondary phase forms so readily, and further exploration is needed.

In light of the fact that the t for $SrNiO_3$ is ~1.08, bulk $SrNiO_3$ is expected to form a hexagonal structure (see Fig. 1A) with face-shared NiO_6 octahedra (15). This structure is not symmetry-matched with traditional perovskite substrates such as $SrTiO_3$ or $LaAlO_3$. First-principles calculations for hexagonal $SrNiO_3$ predict this material to be a half-metallic ferromagnet with promising applications in spintronics and magneto-optical devices (16). In addition, Ni^{4+} has been proposed to be responsible for the high OER performance found in modified nickelate electrocatalysts (17, 18). $SrNiO_3$ with Ni^{4+} is unstable due to its high Gibbs formation energy (19), and as a result, there has been limited success in the synthesis of bulk, hexagonal-structured $SrNiO_3$ (15, 20). In addition, successful epitaxial growth of $SrNiO_{3−δ}$ (where $0 ≤ δ < 1$) thin films has not yet been reported.

Here, we present a study of the synthesis of $SrNiO_{3−δ}$ thin films by oxygen plasma–assisted molecular beam epitaxy (OPA-MBE). By keeping the Sr/Ni ratio at 1:1 during the deposition, we find that instead of forming phase pure $SrNiO_3$, spontaneous phase segregation occurs. Our combined diffraction, spectroscopy, and microscopy dataset reveals that two complementary oxygen-deficient RP phases Sr_2NiO_3 and $SrNi_2O_3$ evolve together, and that these effectively balance the overall film stoichiometry, stabilize the preferred Ni^{2+} oxidation state, and satisfy the epitaxial relationships for both
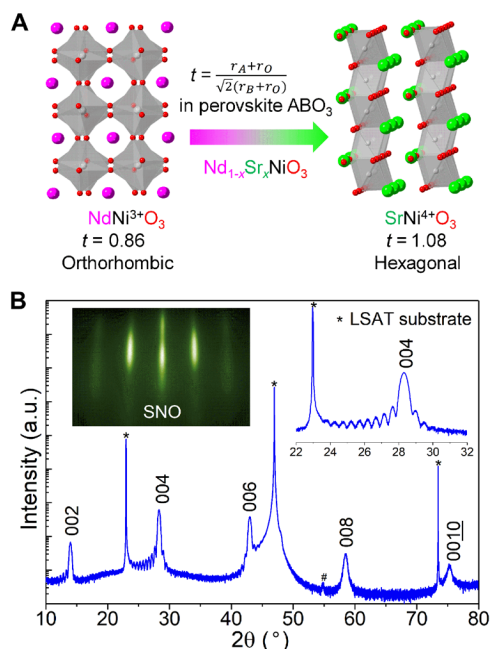
Fig. 1. Epitaxial synthesis of SrNiO$_{3-\delta}$ (SNO) films with a 1:1 Sr/Ni ratio. (A) Schematic crystal structures for bulk NdNi^{3+}O$_3$ and SrNi^{4+}O$_3$. Tolerance factor $t = \frac{r_A + r_O}{\sqrt{2}(r_B + r_O)}$, where r_A, r_B, and r_O are the ionic radius of A and B cations and oxygen, respectively, in a set of ABO$_3$ crystal structures. Sr doping in NdNiO$_3$ (Nd$_{1-x}$Sr$_x$NiO$_3$) would increase t due to the larger ionic radius of Sr^{2+} ion. **(B)** XRD θ-2θ scan of SNO films. The left inset shows the RHEED pattern for an as-grown SNO film on LSAT(001) viewed along the [100] zone axis. The right inset shows the magnified 004 peak with clear thickness fringes. # indicates that the peak originated from our XRD setup. a.u., arbitrary units.

in-plane (IP) film/substrate and out-of-plane (OOP) Sr$_2$NiO$_3$/SrNi$_2$O$_3$ grain interfaces. In addition, a combination of x-ray linear dichroism (XLD) measurements and density functional theory (DFT) calculations reveals the presence of a planar structure in the Sr$_2$NiO$_3$ phase with a large IP orbital occupancy, which may open new avenues for investigation of emergent phenomena in this system.

RESULTS AND DISCUSSION
Epitaxial growth of strontium nickel oxide thin films
Twenty-five-nanometer-thick SrNiO$_{3-\delta}$ (SNO) thin films with a fixed 1:1 Sr/Ni flux ratio (as calibrated by a quartz crystal microbalance at the growth position before growth) were deposited on (001)-oriented (LaAlO$_3$)$_{0.3}$(Sr$_2$AlTaO$_6$)$_{0.7}$ (LSAT) substrates by OPA-MBE. A typical reflection high-energy electron diffraction (RHEED) pattern taken along the [100] zone axis (Fig. 1B) reveals bright, sharp streaks, indicative of a planar surface and an epitaxial orientation with the substrate. The high-resolution x-ray diffraction (XRD) θ to 2θ scan in Fig. 1B shows clear thickness fringes (right inset in Fig. 1B) and strong Bragg peaks, indicating a high extent of crystallographic ordering. A wide-range reciprocal space map (RSM) (fig. S1) confirms the epitaxial relationship. All SNO film peaks in Fig. 1B can be assigned to (00l) reflections with an OOP (c) lattice parameter that is a multiple of 6.3 Å, a value much larger than that of either bulk hexagonal SrNiO$_3$ ($a = 5.355$ Å and $c = 4.86$ Å) or the expected cubic perovskite counterpart ($a = 3.81$ Å) (15, 21). This expanded lattice parameter matches that of Sr$_2$NiO$_3$ (21), for which the Sr/Ni ratio is

clearly not 1:1. Scanning transmission electron microscopy (STEM) images in Fig. 2 reveal that the film consists of layered RP phases. The body-centered symmetry of these compounds results in the absence of diffraction peaks for an odd value of $h + k + l$. Consequently, the XRD indicates an epitaxial RP phase with a c lattice parameter of 12.6 Å aligned perpendicular to the LSAT substrate surface.

Phase segregation in epitaxial SNO films
The high-angle annular dark field (HAADF) STEM image taken along [110] (Fig. 2A) reveals an abrupt interface between the first unit cell (u.c.) and the substrate. Phase segregation is apparent in the thin films consisting of more than 1 u.c. and two different phases can be clearly observed in the STEM image (see the dashed-circle regions). At the onset of SNO film growth, the cubic perovskite substrate can provide a lattice template for nucleation of a NiO$_2$ monolayer followed by a SrO monolayer. This nucleation sequence does not preclude the formation of isolated point defects. As a result, interface engineering and limiting SNO deposition to 1 u.c. in the superlattices could generate novel ground states (such as Ni^{4+}) unobtainable in bulk crystals (22). However, once the SNO film thickness exceeds 1 u.c., the large ionic radius ratio R(Sr^{2+})/R(Ni^{4+}) and the instability of Ni^{4+} could promote phase segregation. Figure 2B shows magnified images of these two different phases that are marked by green and blue rectangles in Fig. 2A. Such spatially distributed, well-separated phases are similar to nanocomposite films reported earlier (23–27). These phases are tentatively assigned to Sr$_2$NiO$_3$ and SrNi$_2$O$_3$ based on the HAADF STEM contrast, the 1:1 Sr/Ni ratio during deposition, and the presence of Ni^{2+} as determined by x-ray photoemission spectroscopy (XPS) and x-ray absorption spectroscopy (XAS) measurements (see Fig. 3). As seen in Fig. 2A, Sr$_2$NiO$_3$ and SrNi$_2$O$_3$ show atomically matched, epitaxial interfaces along the film growth direction. Moreover, both phases show the same c-axis lattice constant (~12.6 Å), consistent with the XRD analysis. The HAADF-STEM images and atomically resolved electron energy loss spectroscopy (EELS) mappings (Fig. 2, C and D) for the two domains viewed along [100] further confirm the phase assignment. Within Sr$_2$NiO$_3$ regions, repeating SrO bilayers and NiO monolayers are clearly resolved along the vertical direction (c axis), as shown in Fig. 2C. Within SrNi$_2$O$_3$ regions, SrO single layers and NiO bilayers are connected along the c axis (Fig. 2D), where a weak signal/interference of Sr in the second Ni layer is also observed, indicating that the phase purity of SrNi$_2$O$_3$ is not as high as that of the Sr$_2$NiO$_3$, or the layer may be more accurately defined as Sr$_{1+x}$Ni$_{2-x}$O$_3$. In addition, localized NiO clusters are observed in the Sr$_{1+x}$Ni$_{2-x}$O$_3$ regions by EELS mappings at lower magnification (fig. S2), which may account for the overall stoichiometry of SrNi$_2$O$_3$.

Although similar structured SrCu$_2$O$_3$ and CaCu$_2$O$_3$ have been reported in previous studies (28–30), the structure of SrNi$_2$O$_3$ has not been predicted or characterized. SrCu$_2$O$_3$ is the first member ($m = 3$) of the homologous series of compounds with a stoichiometry of Sr$_{m-1}$Cu$_{m+1}$O$_{2m}$ ($m = 3, 5, ...$). The Cu-O sheet in SrCu$_2$O$_3$ is made of only Cu-O double chains without any bridging network (29). The CaCu$_2$O$_3$ structure is similar to that of SrCu$_2$O$_3$, but the Cu-O sheets in CaCu$_2$O$_3$ are strongly puckered. On the contrary, Sr$_2$NiO$_3$ films have previously been grown on Sr$_2$TiO$_4$-buffered LaSrAlO$_4$ (100) by pulsed laser deposition (21), indicating that Sr$_2$NiO$_3$ phase is more stable and easier to form than SrNi$_2$O$_3$ phase. Therefore, when the SNO film thickness exceeds 1 u.c., the large ionic radius ratio R(Sr^{2+})/R(Ni^{4+}) and highly unstable Ni^{4+} could promote
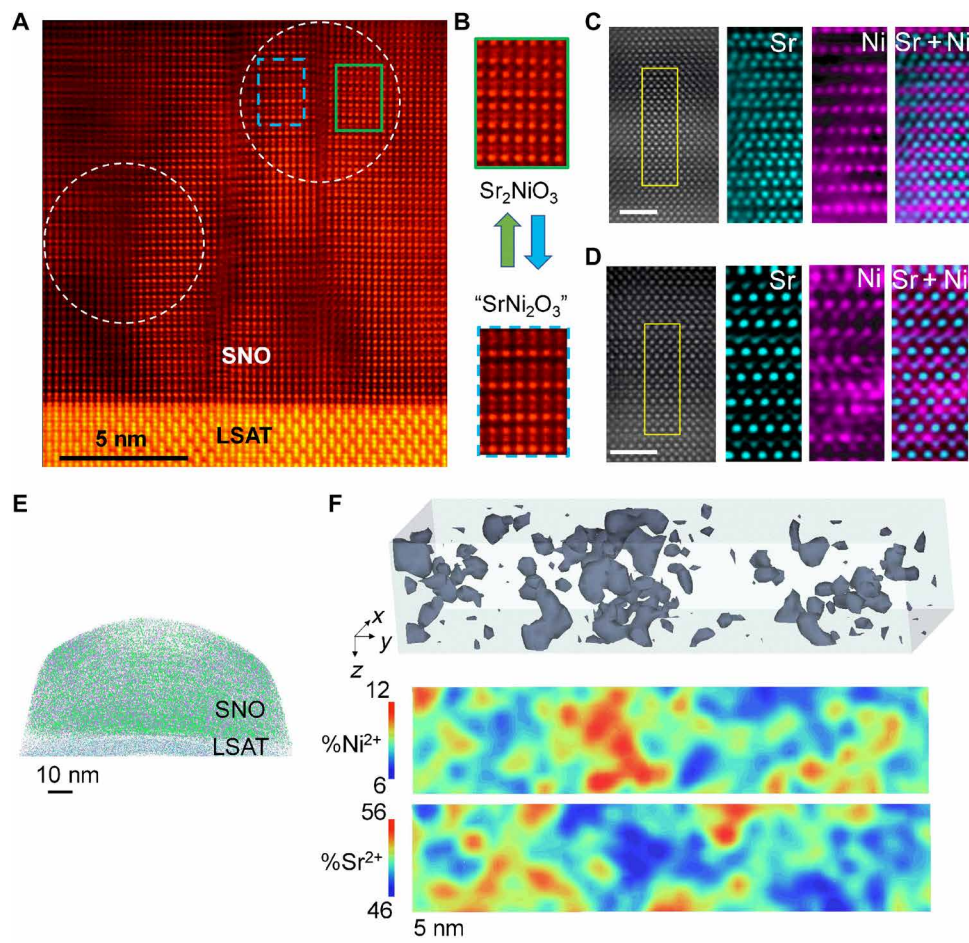
Fig. 2. Phase segregation occurs in SNO films. (**A**) Cross-sectional STEM image of SNO/LSAT along the [110] LSAT direction. Dashed circles clearly show phase segregation. (**B**) Magnified images of the Sr_2NiO_3 phase and the $SrNi_2O_3$ phase marked by green and blue rectangles in (A). (**C** and **D**) Cross-sectional STEM images of two different phases in SNO/LSAT along the [100] LSAT direction. EELS maps (right) from the area marked with a yellow rectangle in the STEM images (left). Scale bar, 2 nm. (**E**) APT tip reconstruction for SNO/LSAT. (**F**) A 3D volume rendering showing regions with greater than 13.5% Ni^{2+} (upper, gray scale). 2D Ni^{2+} (middle) and Sr^{2+} (lower) concentration maps highlighting where spatially localized Ni and Sr enrichment occurs.

the formation of Sr_2NiO_3 phase first. At the same time, a 1:1 Sr/Ni flux ratio could induce the formation of impure $SrNi_2O_3$, leading to the observation of $Sr_{1+x}Ni_{2-x}O_3$ phase and NiO clusters. Sr_2NiO_3 structure can be considered to be a derivative of the layered RP phases ($A_{n+1}B_nO_{3n+1}$, where n is the number of the layers of octahedra in the perovskite-like stack) and can be constructed by removing alternate oxygen ions in the two-dimensional (2D) planes along the IP direction of the A_2BO_4 ($n = 1$) structure. For simplicity, we continue to refer to the mixture of $Sr_{1+x}Ni_{2-x}O_3$ and NiO clusters as $SrNi_2O_3$ and refer to both Sr_2NiO_3 and $SrNi_2O_3$ as reduced RP phases because they have the same c-axis lattice parameter (~12.6 Å). The difference between the epitaxial relationships shown in the two white dotted circles in Fig. 2A may be induced by interfacial defects. In the left circle, Sr planes align well to form a coherent interface between the two different phases. In contrast, the grain boundary defects that are commonly found in metal oxide nanocomposites (*31*) result in poor alignment of Sr planes, as seen in the right circle.

To verify the apparent stabilities of Sr_2NiO_3 and $SrNi_2O_3$, we also deposited and characterized nominally stoichiometric Sr_2NiO_3 and $SrNi_2O_3$ films on LSAT, respectively, by setting the Sr and Ni

fluxes to the desired values (either 2:1 or 1:2). By normalizing the Ni $3p$ XPS spectra in the survey scans, the resulting Sr $3d$ XPS spectra show distinctly different intensities (fig. S3A), quantitatively confirming the different Sr/Ni ratios in these three samples. Moreover, as shown in fig. S3B, the Sr_2NiO_3 film displays a RHEED pattern similar to that of the SNO film with a 1:1 Sr/Ni flux ratio. However, the Sr_2NiO_3 film becomes amorphous once exposed to air. By capping the sample with a 10-nm $LaFeO_3$, the XRD OOP scan of the Sr_2NiO_3 film shows that the diffraction peak is weak and no thickness fringes are observed. In contrast, the RHEED pattern of the $SrNi_2O_3$ film indicates a much rougher surface and a mix of phases. The diffraction peak for the $SrNi_2O_3$ film is also weak, but the peak position is the same as those of the Sr_2NiO_3 film and the $SrNiO_{3-\delta}$ film, indicating that all three films have the same c-axis lattice parameter (~12.6 Å). Therefore, the epitaxial interfaces between Sr_2NiO_3 and $SrNi_2O_3$ columns appear to be responsible for stabilizing these metastable phases to form the vertical "nanocomposite" structures when a 1:1 Sr/Ni flux ratio is used.

The phase-separated reduced RP film was further analyzed by 3D atom probe tomography (3D APT) (Fig. 2E). The 3D elemental
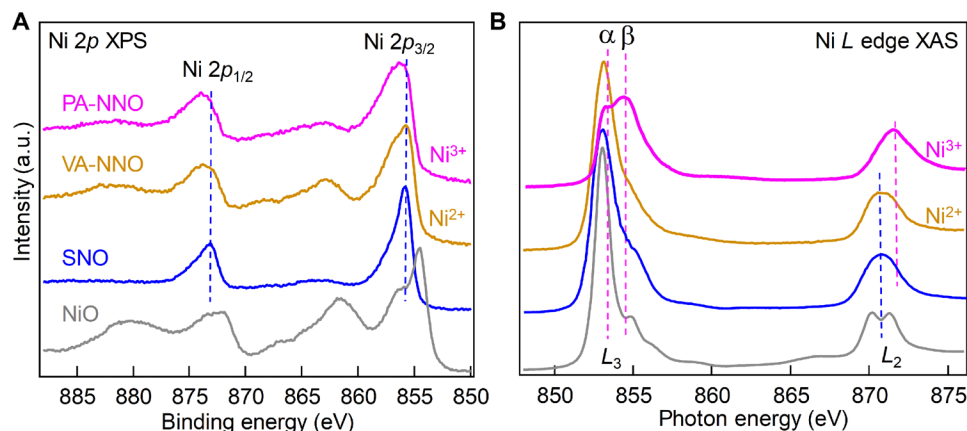
Fig. 3. Spectroscopy results of SNO films. Ni $2p$ XPS (**A**) and Ni L edge XAS (**B**) of SNO films. The reference spectra for Ni^{2+} and Ni^{3+} were measured using a vacuum-annealed $NdNiO_{3-\delta}$ film (VA-NNO) and a plasma-annealed $NdNiO_3$ film (PA-NNO), respectively, both grown on $SrTiO_3(001)$. The spectrum for a NiO film grown on MgO (001) is included for comparison. The blue dashed lines in (A) denote the Ni $2p_{1/2}$ and Ni $2p_{3/2}$ peak positions of SNO films. The purple and blue dashed lines in (B) are guidelines for peak positions.

reconstruction was accomplished through assignment of ionic species from the mass spectra to best reproduce the SNO stoichiometry (fig. S4). In general, the major Ni and Sr species were Ni^{2+} at 29 to 32 Da and Sr^{2+} at 42 to 44 Da. Here, 2+ is not the valence of Ni in the solid, but rather the mass-to-charge ratio of the ion detected in APT. The minor isotope ^{64}Ni interferes with $^{16}O_2{}^{1+}$ at 32 Da and is excluded from analysis of the Ni^{2+} species. Additional polyatomic/isobaric interferences for the Ni^{2+} and Sr^{2+} species were not observed. In turn, the Ni^{2+} and Sr^{2+} ionic species were used in evaluating the Ni and Sr distribution for simplicity. Potential elemental partitioning within a small subvolume of the SNO layer was visualized in 3D using iso-concentration surfaces of the major ionic species Ni^{2+} and Sr^{2+} species. Ni-rich regions are visualized using iso-concentration surfaces exceeding the average Ni^{2+} concentration (e.g., 13.5 ionic % Ni^{2+}) in turn enabling observation of more Ni-rich phases (Fig. 2F). Ni-rich regions within the SNO matrix are generally circuitous and randomly distributed in space. 2D concentration maps (middle panel and lower panel of Fig. 2F) further highlight Ni-rich regions correlated to Sr-poor regions, strongly supporting our proposed Sr_2NiO_3 and $SrNi_2O_3$ model.

In situ x-ray photoemission and ex situ absorption spectroscopy

Figure 3A shows Ni $2p$ XPS spectra of a representative SNO film and three reference samples. Surface charging was consistently observed, and all spectra were shifted so that the O $1s$ peaks fall at 530 eV. Oxygen plasma annealing has been shown to be effective at healing oxygen vacancies in oxide thin films (32). Accordingly, a plasma-nnealed $NdNiO_3$ film (PA-NNO) was used as a Ni^{3+} standard and a vacuum-annealed $NdNiO_{3-\delta}$ film (VA-NNO) was used as a Ni^{2+} reference (33). The Ni $2p$ XPS spectrum for PA-NNO consists of two dominant spin-orbit split features at ~856.3 and 873.9 eV, respectively. These peaks shift to lower binding energy in VA-NNO, consistent with the previous reports (34). These two peaks are significantly narrower in SNO than in PA-NNO, and the binding energies are nearly the same as those for VA-NNO, suggesting the same Ni^{2+} valence in the two films. In addition, the Ni L edge XAS spectrum for SNO (Fig. 3B) shows the same shape and peak positions as the spectrum for VA-NNO. However, these differ significantly from those of PA-NNO. There are two distinct peaks α and β

located at 853.3 and 854.3 eV, respectively, at the Ni L_3 edge in the PA-NNO spectrum and a single feature at ~871.6 eV at the Ni L_2 edge. In contrast, SNO shows one asymmetric feature located at ~853 eV at the Ni L_3 edge and the Ni L_2 edge is clearly shifted to lower photon energy at ~870.6 eV. Previous studies show that increasing oxygen nonstoichiometry results in a gradual change in valence from Ni^{3+} to Ni^{2+} and the Ni L_3 edge is marked by an increase (decrease) in the intensity of peak α (β) as well as a shift to lower (higher) photon energy (35–37). This change is clearly seen at the Ni L_3 edge in Fig. 3B. Together, the Ni XPS and XAS spectra support the presence of divalent Ni in the SNO films. However, it should be noted that the spectra of VA-NNO and SNO are different from that of the Ni^{2+}-containing standard, a NiO film grown on MgO(001). This difference is most likely due to the significantly different local atomic (RP versus rock salt) structures and bonding configurations.

As with the Cu L edge spectra in cuprates (38), peak β in the Ni L edge (Fig. 3B) is indicative of ligand holes formed as a result of Ni $3d$–O $2p$ hybridization. The diminution of peak β in SNO and VA-NNO implies that the Ni $3d$–O $2p$ hybridization strength decreases relative to PA-NNO. Owing to the strong hybridization between Ni $3d$ and O $2p$ bands at the Fermi level, O K edge XAS becomes another useful way to probe the valence of Ni with adjacent ligand holes. Figure 4A shows the O K edge XAS for the SNO film and reference samples. The spectra are normalized to zero and unity at the O K pre-edge and post-edge, respectively, and the spectra are shifted vertically for clarity. The spectra for PA-NNO and VA-NNO agree well with those reported in the literature (5, 37, 39, 40). For PA-NNO, a sharp pre-edge peak (marked by a dashed purple line) centered at ~528 eV, a broad feature near 535 eV, and a doublet at 540 to 545 eV reveal hybridization of the O $2p$ band with Ni $3d$, Nd $4f$, and Ni $4sp$ bands, respectively. The sharp pre-edge peak at ~528 eV in PA-NNO originates from the $3d^8\underline{L} \rightarrow \underline{c}3d^8$ (Ni^{3+}) transition, where $\underline{L}$ denotes a ligand hole and $\underline{c}$ denotes an O $1s$ core hole (41). The intensity of the pre-edge peak is directly related to the ligand hole density, which in turn strongly affects transport behavior in nickelates films (8, 36, 42, 43). As seen in Fig. 4B and fig. S5, PA-NNO shows metallic bulk-like ρ-T behavior with low resistivity of ~3.2×10^{-4} ohm·cm at 300 K. In sharp contrast, the pre-edge peak is strongly suppressed in SNO, revealing the insulating behavior at
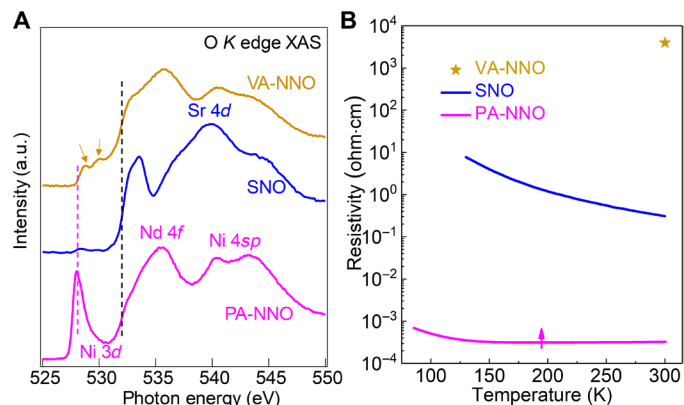
Fig. 4. O K edge XAS and electrical transport of SNO. (**A**) O K edge XAS for PA-NNO, SNO, and VA-NNO films measured at room temperature. (**B**) Temperature-dependent resistivity of these three samples. The purple arrow denotes the metal-insulator transition point (T_{MI}).

300 K. Moreover, the O K edge spectrum for VA-NNO exhibits notable changes compared with PA-NNO, especially in the Ni $3d$ band region. For VA-NNO, the pre-edge peak located at ~528 eV disappears and two small features appear at ~528.8 and ~ 530.1 eV (marked by two yellow arrows in Fig. 4A), which match well with those observed in LaNi^{2+}O$_{2.5}$ (44, 45). Even though Ni ions in both SNO with its mixed phases and VA-NNO are both Ni^{2+}, their O K edge XAS spectra are quite distinct due to differences in band structure that also greatly affect conductivity (see Fig. 4B). Thus, the local coordination environment and associated electronic structure of Ni atoms in SNO with its mix of Sr$_2$NiO$_3$ and SrNi$_2$O$_3$ are different from that found in VA-NNO and LaNiO$_{2.5}$, in which Ni atoms are in a square-planar structure with chains of NiO$_6$ octahedra (O_h) and NiO$_4$ square-planar (D_{4h}) configurations (44, 46, 47).

Orbital polarization in SNO films

We also investigated the orbital polarization in the SNO films using XLD. The $d_{x^2-y^2}$ and the $d_{3z^2-r^2}$ orbitals can be probed independently by using IP and OOP x-ray polarization, respectively. The absorption spectra for these two polarizations are shown in Fig. 5A. The XLD (defined here as $I_{EIP} - I_{EOOP}$) indicates the predominant occupation of the $d_{x^2-y^2}$ IP orbital, suggesting the atomic orbital scheme shown in the inset in Fig. 5A. To quantify the orbital polarization (P), we first calculate the ratio of unoccupied states, r (48)

$$r = \frac{h_{3z^2-r^2}}{h_{x^2-y^2}} = \frac{3 I_{E_{OOP}}}{4 I_{E_{IP}} - I_{E_{OOP}}} \qquad (1)$$

Here, h_i is the number of holes in orbital i and I_j is the integrated L edge spectral intensity with polarization j. We obtain $r = 1.12$ by integrating the spectra over the range 850 to 875 eV. This hole ratio value is comparable to previously reported values of $r = 1.19$ for nickel oxide superlattices in tension and $r = 1.05$ resulting from spatial confinement in LaAlO$_3$/LNO superlattices (48, 49). The r value can be used to evaluate the orbital polarization, P (50)

$$P = \left(\frac{4}{n_{e_g}} - 1\right)\frac{1-r}{1+r} \qquad (2)$$

where n_{e_g} is the total number of e_g electrons. We obtain a value of $P = 5.7\%$ for our SNO films if $n_{e_g} = 2$, as expected for Ni^{2+} ($3d^8$).

To better understand the XLD results in light of the coexistence of Sr$_2$NiO$_3$ and SrNi$_2$O$_3$ in SNO/LSAT, we conducted first-principles calculations (see Materials and Methods for details). We calculated the density of states (DOS) of four different structures: Sr$_2$NiO$_4$ (SNO_214), pyramidal Sr$_2$NiO$_3$ (SNO_213 pyramid), planar Sr$_2$NiO$_3$ (SNO_213 planar), and SrNi$_2$O$_3$ (SNO_123). The calculated minimum-energy structures are shown in Fig. 5B. The calculated c-axis lattice parameters of these four different structures are 12.24 Å for SNO_214, 12.86 Å for SNO_213 pyramid, 12.57 Å for SNO_213 planar, and 10.39 Å for SNO_123, respectively. However, experimental results (XRD and STEM) show that both phases have the same c-axis lattice constant (~12.6 Å). The Sr$_2$NiO$_3$ phase has a calculated lattice parameter closest to our measured value, whereas the SrNi$_2$O$_3$ phase has a much-reduced lattice parameter compared to the experimental value. Partial Sr intermixing within the Ni planes (Sr$_{1+x}$Ni$_{2-x}$O$_3$) can be invoked to maintain a 12.6-Å c lattice parameter and an epitaxial relationship between the two phases. Figure 5C shows the partial DOS (PDOS) results from which the orbital polarization in each structure can be obtained. For SNO_214 (Ni^{4+}), there is no bandgap and the IP orbital has a larger bandwidth and a slightly lower average energy than the OOP orbital. For SNO_213 pyramid (Ni^{2+}), the IP orbital has a higher energy than the OOP orbital and a large Δe_g (~0.7 eV) is observed. For SNO_213 planar (Ni^{2+}), $\Delta e_g = 0$, and it is almost fully polarized with the OOP orbital unoccupied, in qualitative agreement with our XLD measurements. SNO_123 (Ni^{2+}) shows a clear orbital polarization and the IP orbital is mainly unoccupied, which is the opposite of SNO_213 planar. Because of the phase segregation that occurs in our SNO films, the orbital polarization in SNO_123 will partially cancel out that in SNO_213. In addition, the phase purity of SrNi$_2$O$_3$ is not as high as that of the Sr$_2$NiO$_3$. Although it will not affect the net orbital polarization of our SNO films, which is dominated by the contribution from the SNO_213 phase, the orbital polarization P for our SNO film ($P \approx 5.7\%$) is smaller than that found in the square-planar phase R$_4$Ni$_3$O$_8$ (R = La, Pr) obtained by hydrogen reduction (51), in which ~70% of the holes occupy the $d_{x^2-y^2}$ IP orbital. This value is the highest published in the literature for Ni-based complex oxides (48–50, 52). Although a large IP orbital occupation has been observed in our SNO film, it should be mentioned here that the infinite NiO$_2$ plane in the SNO_213 planar structure is along the OOP direction, different from the IP infinite NiO$_2$ planes shown in superconducting Nd$_{0.8}$Sr$_{0.2}$NiO$_2$ films (11). Moreover, spectroscopy data demonstrate the $3d^8$ configuration in our insulating SNO films, while a predicted $3d^9$ configuration should exist in the superconducting Nd$_{0.8}$Sr$_{0.2}$NiO$_2$ films (11).

In summary, our study demonstrates that the end member of phase pure SrNi^{4+}O$_3$ thin films in Nd$_{1-x}$Sr$_x$NiO$_3$ where $x = 1$ cannot be stabilized as a pseudo-cubic structure by epitaxial growth. However, suitable perovskite substrates can be effective templates for the nucleation and growth of structurally compatible oxygen-deficient RP phases, Sr$_2$NiO$_3$ and SrNi$_2$O$_3$. Their coexistence effectively satisfies an overall Sr/Ni ratio of 1:1, leading to an epitaxial c-axis–oriented nanocomposite. The dynamic phase segregation process that occurs during MBE growth of this material requires high cation diffusion rates and extensive vertical redistribution. Although the exact growth mechanism remains to be elucidated, our observations indicate that this system presents a fascinating testbed for an unusual kind of film nucleation that appears to be driven by the high stability of a particular cation valence, Ni^{2+}. We envision that this kind of
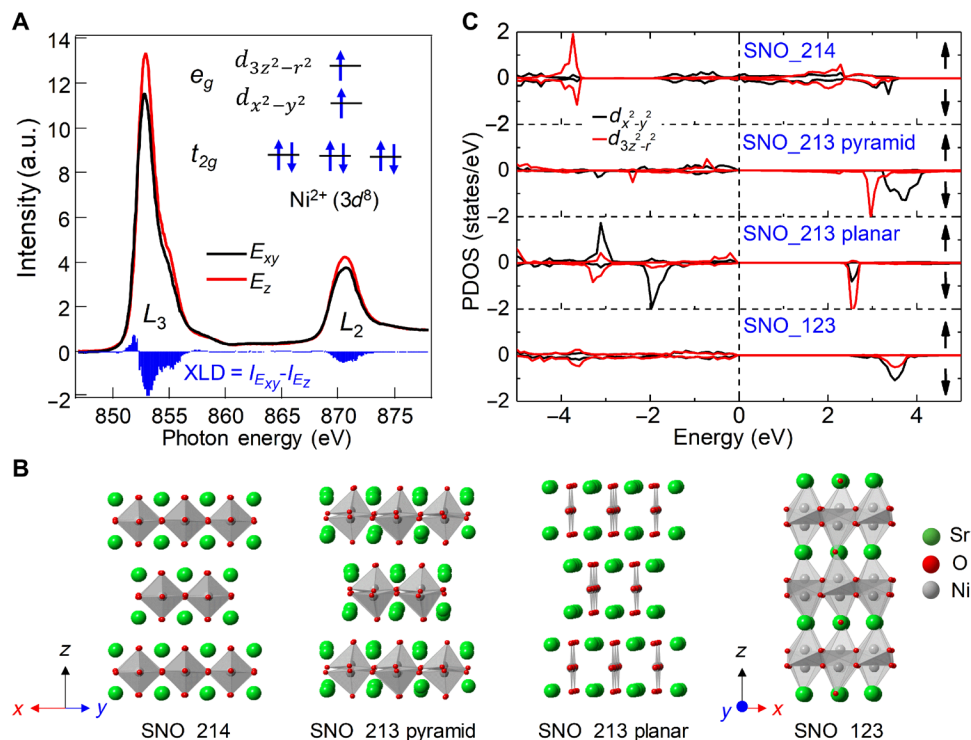
Fig. 5. Orbital polarization in SNO films. (A) Polarization-dependent XAS across the Ni L edge for SNO/LSAT(001). The inset shows a sketch of the engineered orbital and spin states, which forms the electronic configuration (Ni^{2+}, $3d^8$) and orbital polarization ($n_{dx2-y2} > n_{d3z2-r2}$). **(B)** Schematic of the crystalline structures of Sr$_2$NiO$_4$ (SNO_214), pyramid Sr$_2$NiO$_3$ (SNO_213 pyramid), planar Sr$_2$NiO$_3$ (SNO_213 planar), and SrNi$_2$O$_3$ (SNO_123). **(C)** Partial density of states (PDOS) of these four different systems. The Fermi level (the black dashed line) is placed at 0 eV. The black arrows denote the spin state.

spontaneous phase segregation and RP faults may occur during the synthesis of Sr-doped RNiO$_3$ where the Sr doping level is high. The presence of randomly distributed, mixed RP or reduced RP phases adds additional synthesis challenges in studying superconductivity but may open other avenues to explore the emergent phenomena in nickelates.

MATERIALS AND METHODS
Sample growth
SNO thin films (~25 nm) were grown on (001)-oriented LSAT substrates by OPA-MBE. Sr and Ni were evaporated from the effusion cells, and the evaporation rates were calibrated using a quartz crystal oscillator. The Sr (Ni) fluxes were calibrated by growing SrTiO$_3$ (LaNiO$_3$) films on (001)-oriented SrTiO$_3$ substrate, respectively. Once we obtain stable RHEED oscillations, the exact flux was extracted from the period (deposition time per unit cell) and used for SNO film growth. The substrate temperature was set to 700°C, and the activated oxygen partial pressure was kept at ~3×10^{-6} torr during growth. In situ RHEED was used to monitor the overall growth rate, and surface crystallography and structure. After growth, the sample was cooled down to room temperature at 30°C/min under activated oxygen. Two 12-nm-thick NdNiO$_3$ films grown on (001)-oriented Nb-doped SrTiO$_3$ substrate were annealed in oxygen plasma and vacuum, respectively, to use as reference samples for comparing the Ni XPS and XAS spectra with SNO. One 20-u.c.-thick NiO film grown on MgO (001) substrate was also used as reference sample.

XPS and XAS measurements
In situ XPS measurements were carried out on the as-grown samples. A low-energy electron flood gun was used to neutralize the charging effect. The TEY XAS measurements of the Ni L edge and O K edge were performed at the Singapore Synchrotron Light Source and the photoemission station at Beijing Synchrotron Radiation Facility of Institute of High Energy Physics, Chinese Academy of Sciences. All XPS and XAS were measured with the samples at 300 K. The x-ray incident angles 90° and 30° correspond to IP (E_{xy}) and OOP (E_z) polarizations, respectively.

Sample characterization
A high-resolution x-ray diffractometer (Rigaku SmartLab) was used to measure the lattice structure. HAADF images were obtained by using a probe-corrected ARM200F (JEOL, Tokyo, Japan) STEM operated at 200 kV using a ~1-Å probe with a 27.5-mrad convergence semiangle and an 82-mrad collection inner angle. EELS mapping was performed using a probe-corrected GrandARM-300F (JEOL, Tokyo, Japan) STEM operating at 300 kV, using a ~1-Å probe with a 29-mrad convergence semiangle and a ~113-mrad spectrometer collection inner angle.

Conventional focused-ion beam milling techniques were applied to fabricate APT tips using a dual-beam scanning electron microscope (Thermo Fisher Scientific Helios Nanolab 600i) (53). A description of the preparation techniques, including protective coatings used, is provided in the Supplementary Materials. APT was performed using a CAMECA local electrode atom probe (LEAP) 4000 X-HR at a base temperature and pressure of 40 K and < 3×10^{-11} torr, respectively.

The detection efficiency is nominally 36%. Field evaporation of ions from the specimen was induced by a 355-nm–wavelength picosecond laser at a pulse repetition rate of 125 kHz. A detection rate of 0.003 to 0.004 ions per pulse was maintained by varying the applied specimen voltage. The SNO film was captured in three of the four tips, using laser pulse energies between 60 and 160 pJ. One tip is described in detail in the text, representative of observations found across all samples. Data were reconstructed in 3D by using the integrated visualization and analysis software (IVAS 3.8.2) developed by CAMECA (Madison, WI). An average atomic volume of 0.06 nm^3 atom^{-1} was specified in the 3D reconstruction, representing the atomic density of a SrNiO$_3$ lattice [i.e., using the theoretically calculated density of 5.50 g cm^{-3} determined by Jain et al. (54) (SrNiO$_3$ ID # mp-762506)]. The reconstructions were further optimized to reproduce flat SNO-LSAT interfaces, primarily by adjusting the image compression factor. A voxel size of 1.0 nm by 1.0 nm by 1.0 nm and delocalization of 3.0 nm by 3.0 nm by 1.5 nm were applied. Chemical visualization and analysis of the SNO film were enabled through assignment of Sr-, Ni-, and O-ionic species to the mass spectra (fig. S4), which yielded an average elemental composition of the SNO matrix of ~20.9% Ni, ~36.9% Sr, and ~42.2% O. IP transport measurements were performed in a van der Pauw geometry using a Hall measurement system in the temperature range 85 to 310 K.

DFT calculations

The DFT calculations are carried out using the Vienna ab initio simulation package (55). The atomic potentials are approximated by the projected augmented wave method (56), with Sr $4s^24p^65s^2$, Ni $3d^94s^1$, and O $2s^22p^6$ reference configurations. The GGA-PBEsol functional was used as an approximation to the exchange correlation (57). The DFT + U method with U = 6 eV was used to correct the underestimation of on-site Coulomb interaction between the Ni $3d$ electrons (58). The Kohn-Sham wave functions are represented by a plane wave basis set with an energy cutoff of 550 eV. The Brillouin zone is sampled with an 888 Monkhorst-Pack grid. The forces are reduced to less than 10^{-3} eV/Å when relaxing the structures.

SUPPLEMENTARY MATERIALS

Supplementary material for this article is available at http://advances.sciencemag.org/cgi/content/full/7/10/eabe2866/DC1

REFERENCES AND NOTES

1. G. Catalan, Progress in perovskite nickelate research. Phase Transit. **81**, 729–749 (2008).
2. S. Catalano, M. Gibert, J. Fowlie, J. Íñiguez, J.-M. Triscone, J. Kreisel, Rare-earth nickelates RNiO$_3$: Thin films and heterostructures. Rep. Prog. Phys. **81**, 046501 (2018).
3. S. Middey, J. Chakhalian, P. Mahadevan, J. W. Freeland, A. J. Millis, D. D. Sarma, Physics of ultrathin films and heterostructures of rare-earth nickelates. Annu. Rev. Mat. Res. **46**, 305–334 (2016).
4. R. Scherwitzl, P. Zubko, I. G. Lezama, S. Ono, A. F. Morpurgo, G. Catalan, J.-M. Triscone, Electric-field control of the metal-insulator transition in ultrathin NdNiO$_3$ films. Adv. Mater. **22**, 5517–5520 (2010).
5. J. Liu, M. Kargarian, M. Kareev, B. Gray, P. J. Ryan, A. Cruz, N. Tahir, Y.-D. Chuang, J. Guo, J. M. Rondinelli, J. W. Freeland, G. A. Fiete, J. Chakhalian, Heterointerface engineered electronic and magnetic phases of NdNiO$_3$ thin films. Nat. Commun. **4**, 2714 (2013).
6. E. Mikheev, A. J. Hauser, B. Himmetoglu, N. E. Moreno, A. Janotti, C. G. Van de Walle, S. Stemmer, Tuning bad metal and non-Fermi liquid behavior in a Mott material: Rare-earth nickelate thin films. Sci. Adv. **1**, e1500797 (2015).
7. J. R. Petrie, V. R. Cooper, J. W. Freeland, T. L. Meyer, Z. Zhang, D. A. Lutterman, H. N. Lee, Enhanced bifunctional oxygen catalysis in strained LaNiO$_3$ perovskites. J. Am. Chem. Soc. **138**, 2488–2491 (2016).
8. L. Wang, K. A. Stoerzinger, L. Chang, J. Zhao, Y. Li, C. S. Tang, X. Yin, M. E. Bowden, Z. Yang, H. Guo, L. You, R. Guo, J. Wang, K. Ibrahim, J. Chen, A. Rusydi, J. Wang, S. A. Chambers, Y. Du, Tuning bifunctional oxygen electrocatalysts by changing the A-site rare-earth element in perovskite nickelates. Adv. Funct. Mater. **28**, 1803712 (2018).
9. L. Chang, L. Wang, L. You, Z. Yang, A. Abdelsamie, Q. Zhang, Y. Zhou, L. Gu, S. A. Chambers, J. Wang, Tuning photovoltaic performance of perovskite nickelates heterostructures by changing the A-site rare-earth element. ACS Appl. Mater. Interfaces **11**, 16191–16197 (2019).
10. J. Liu, E. Jia, L. Wang, K. A. Stoerzinger, H. Zhou, C. S. Tang, X. Yin, X. He, E. Bousquet, M. E. Bowden, A. T. S. Wee, S. A. Chambers, Y. Du, Tuning the electronic structure of LaNiO$_3$ through alloying with strontium to enhance oxygen evolution activity. Adv. Sci. **6**, 1901073 (2019).
11. D. Li, K. Lee, B. Y. Wang, M. Osada, S. Crossley, H. R. Lee, Y. Cui, Y. Hikita, H. Y. Hwang, Superconductivity in an infinite-layer nickelate. Nature **572**, 624–627 (2019).
12. Q. Li, C. He, J. Si, X. Zhu, Y. Zhang, H.-H. Wen, Absence of superconductivity in bulk Nd$_{1-x}$Sr$_x$NiO$_2$. Commun. Mater. **1**, 16 (2020).
13. B.-X. Wang, H. Zheng, E. Krivyakina, O. Chmaissem, P. P. Lopes, J. W. Lynn, L. C. Gallington, Y. Ren, S. Rosenkranz, J. F. Mitchell, D. Phelan, Synthesis and characterization of bulk Nd$_{1-x}$Sr$_x$NiO$_2$ and Nd$_{1-x}$Sr$_x$NiO$_3$. Phys. Rev. Materials **4**, 084409 (2020).
14. K. Lee, B. H. Goodge, D. Li, M. Osada, B. Y. Wang, Y. Cui, L. F. Kourkoutis, H. Y. Hwang, Aspects of the synthesis of thin film superconducting infinite-layer nickelates. APL Mater. **8**, 041107 (2020).
15. Y. Takeda, T. Hashino, H. Miyamoto, F. Kanamaru, S. Kume, M. Koizumi, Synthesis of SrNiO$_3$ and related compound, Sr$_2$Ni$_2$O$_5$. J. Inorg. Nucl. Chem. **34**, 1599–1601 (1972).
16. G.-Y. Chen, C.-L. Ma, D. Chen, Y. Zhu, Robust half-metallicity of hexagonal SrNiO$_3$. J. Solid State Chem. **233**, 438–443 (2016).
17. J. G. Lee, J. Hwang, H. J. Hwang, O. S. Jeon, J. Jang, O. Kwon, Y. Lee, B. Han, Y.-G. Shul, A new family of perovskite catalysts for oxygen-evolution reaction in alkaline media: BaNiO$_3$ and BaNi$_{0.83}$O$_{2.5}$. J. Am. Chem. Soc. **138**, 3541–3547 (2016).
18. N. Li, D. K. Bediako, R. G. Hadt, D. Hayes, T. J. Kempa, F. von Cube, D. C. Bell, L. X. Chen, D. G. Nocera, Influence of iron doping on tetravalent nickel content in catalytic oxygen evolving films. Proc. Natl. Acad. Sci. U.S.A. **114**, 1486–1491 (2017).
19. F. Calle-Vallejo, J. I. Martínez, J. M. García-Lastra, M. Mogensen, J. Rossmeisl, Trends in stability of perovskite oxides. Angew. Chem. Int. Ed. **49**, 7699–7701 (2010).
20. M. Zinkevich, Constitution of the Sr–Ni–O system. J. Solid State Chem. **178**, 2818–2824 (2005).
21. M. Ohtani, H. Kishida, K. Hirota, H. Sakurada, N. Kawamoto, Y. Murakami, K. Ueno, J. Matsuno, Y. Okimoto, T. Makino, Y. Segawa, Y. Tokura, D. Shindo, H. Okamoto, M. Kawasaki, Sr$_2$TMO$_3$ (TM = Ni, Co) compounds with 1D TM–O chains. Adv. Mater. **18**, 2541–2544 (2006).
22. L. Wang, Z. Yang, M. E. Bowden, J. W. Freeland, P. V. Sushko, S. R. Spurgeon, B. Matthews, W. S. Samarakoon, H. Zhou, Z. Feng, M. H. Engelhard, Y. Du, S. A. Chambers, Hole-trapping-induced stabilization of Ni^{4+} in SrNiO$_3$/LaFeO$_3$ superlattices. Adv. Mater. **32**, 2005003 (2020).
23. Q. Zhan, R. Yu, S. P. Crane, H. Zheng, C. Kisielowski, R. Ramesh, Structure and interface chemistry of perovskite-spinel nanocomposite thin films. Appl. Phys. Lett. **89**, 172902 (2006).
24. J. L. MacManus-Driscoll, P. Zerrer, H. Wang, H. Yang, J. Yoon, A. Fouchet, R. Yu, M. G. Blamire, Q. Jia, Strain control and spontaneous phase ordering in vertical nanocomposite heteroepitaxial thin films. Nat. Mater. **7**, 314–320 (2008).
25. H. Yang, H. Wang, J. Yoon, Y. Wang, M. Jain, D. M. Feldmann, P. C. Dowden, J. L. MacManus-Driscoll, Q. Jia, Vertical interface effect on the physical properties of self-assembled nanocomposite epitaxial films. Adv. Mater. **21**, 3794–3798 (2009).
26. A. Chen, Z. Bi, C.-F. Tsai, J. Lee, Q. Su, X. Zhang, Q. Jia, J. L. MacManus-Driscoll, H. Wang, Tunable low-field magnetoresistance in (La$_{0.7}$Sr$_{0.3}$MnO$_3$)$_{0.5}$:(ZnO)$_{0.5}$ self-assembled vertically aligned nanocomposite thin films. Adv. Funct. Mater. **21**, 2423–2429 (2011).
27. A. Chen, J.-M. Hu, P. Lu, T. Yang, W. Zhang, L. Li, T. Ahmed, E. Enriquez, M. Weigand, Q. Su, H. Wang, J.-X. Zhu, J. L. MacManus-Driscoll, L.-Q. Chen, D. Yarotski, Q. Jia, Role of scaffold network in controlling strain and functionalities of nanocomposite films. Sci. Adv. **2**, e1600245 (2016).
28. C. L. Teske, H. Müller-Buschbaum, Über erdalkalimetall-oxocuprate. I. Zur Kenntnis von CaCu$_2$O$_3$. Z. Anorg. Allg. Chem. **370**, 134–143 (1969).
29. Z. Hiroi, M. Azuma, M. Takano, Y. Bando, A new homologous series Sr$_{n-1}$Cu$_{n+1}$O$_{2n}$ found in the SrO-CuO system treated under high pressure. J. Solid State Chem. **95**, 230–238 (1991).
30. N. J. C. Ingle, R. H. Hammond, M. R. Beasley, Molecular beam epitaxial growth of SrCu$_2$O$_3$: Metastable structures and the role of epitaxy. J. Appl. Phys. **91**, 6371–6378 (2002).
31. A. Chen, Q. Su, H. Han, E. Enriquez, Q. Jia, Metal oxide nanocomposites: A perspective from strain, defect, and interface. Adv. Mater. **31**, 1803241 (2019).
32. L. Wang, Y. Du, P. V. Sushko, M. E. Bowden, K. A. Stoerzinger, S. M. Heald, M. D. Scafetta, T. C. Kaspar, S. A. Chambers, Hole-induced electronic and optical transitions in La$_{1-x}$Sr$_x$FeO$_3$ epitaxial thin films. Phys. Rev. Mater. **3**, 025401 (2019).

33. L. Wang, S. Dash, L. Chang, L. You, Y. Feng, X. He, K.-j. Jin, Y. Zhou, H. Guan Ong, P. Ren, S. Wang, L. Chen, J. Wang, Oxygen vacancy induced room-temperature metal–insulator transition in nickelate films and its potential application in photovoltaics. *ACS Appl. Mater. Interfaces* **8**, 9769–9776 (2016).

34. J. Shi, Y. Zhou, S. Ramanathan, Colossal resistance switching and band gap modulation in a perovskite nickelate by electron doping. *Nat. Commun.* **5**, 4860 (2014).

35. J. W. Freeland, M. Van Veenendaal, J. Chakhalian, Evolution of electronic structure across the rare-earth RNiO₃ series. *J. Electron Spectros. Relat. Phenomena* **208**, 56–62 (2016).

36. L. Wang, L. Chang, X. Yin, L. You, J.-L. Zhao, H. Guo, K. Jin, K. Ibrahim, J. Wang, A. Rusydi, J. Wang, Self-powered sensitive and stable UV-visible photodetector based on GdNiO₃/Nb-doped SrTiO₃ heterojunctions. *Appl. Phys. Lett.* **110**, 043504 (2017).

37. M. Kotiuga, Z. Zhang, J. Li, F. Rodolakis, H. Zhou, R. Sutarto, F. He, Q. Wang, Y. Sun, Y. Wang, N. A. Aghamiri, S. B. Hancock, L. P. Rokhinson, D. P. Landau, Y. Abate, J. W. Freeland, R. Comin, S. Ramanathan, K. M. Rabe, Carrier localization in perovskite nickelates from oxygen vacancies. *Proc. Natl. Acad. Sci. U.S.A.* **116**, 21992–21997 (2019).

38. X. Yin, S. Zeng, T. Das, G. Baskaran, T. C. Asmara, I. Santoso, X. Yu, C. Diao, P. Yang, M. B. H. Breese, T. Venkatesan, H. Lin, Ariando, A. Rusydi, Coexistence of midgap antiferromagnetic and mott states in undoped, hole-and electron-doped ambipolar cuprates. *Phys. Rev. Lett.* **116**, 197002 (2016).

39. J. Suntivich, W. T. Hong, Y.-L. Lee, J. M. Rondinelli, W. Yang, J. B. Goodenough, B. Dabrowski, J. W. Freeland, Y. Shao-Horn, Estimating hybridization of transition metal and oxygen states in perovskites from O K-edge x-ray absorption spectroscopy. *J. Phys. Chem. C* **118**, 1856–1863 (2014).

40. N. Palina, L. Wang, S. Dash, X. Yu, M. B. H. Breese, J. Wang, A. Rusydi, Investigation of the metal–insulator transition in NdNiO₃ films by site-selective x-ray absorption spectroscopy. *Nanoscale* **9**, 6094–6102 (2017).

41. J. Chakhalian, J. M. Rondinelli, J. Liu, B. A. Gray, M. Kareev, E. J. Moon, N. Prasai, J. L. Cohn, M. Varela, I. C. Tung, M. J. Bedzyk, S. G. Altendorf, F. Strigari, B. Dabrowski, L. H. Tjeng, P. J. Ryan, J. W. Freeland, Asymmetric orbital-lattice interactions in ultrathin correlated oxide films. *Phys. Rev. Lett.* **107**, 116805 (2011).

42. Y. Cao, X. Liu, M. Kareev, D. Choudhury, S. Middey, D. Meyers, J.-W. Kim, P. J. Ryan, J. W. Freeland, J. Chakhalian, Engineered Mott ground state in a LaTiO₃₊δ/LaNiO₃ heterostructure. *Nat. Commun.* **7**, 10418 (2016).

43. M. Golalikhani, Q. Lei, R. U. Chandrasena, L. Kasaei, H. Park, J. Bai, P. Orgiani, J. Ciston, G. E. Sterbinsky, D. A. Arena, P. Shafer, E. Arenholz, B. A. Davidson, A. J. Millis, A. X. Gray, X. X. Xi, Nature of the metal-insulator transition in few-unit-cell-thick LaNiO₃ films. *Nat. Commun.* **9**, 2206 (2018).

44. M. Abbate, G. Zampieri, F. Prado, A. Caneiro, J. M. Gonzalez-Calbet, M. Vallet-Regi, Electronic structure and metal-insulator transition in LaNiO₃₋δ. *Phys. Rev. B* **65**, 155101 (2002).

45. M. Hepting, D. Li, C. J. Jia, H. Lu, E. Paris, Y. Tseng, X. Feng, M. Osada, E. Been, Y. Hikita, Y.-D. Chuang, Z. Hussain, K. J. Zhou, A. Nag, M. Garcia-Fernandez, M. Rossi, H. Y. Huang, D. J. Huang, Z. X. Shen, T. Schmitt, H. Y. Hwang, B. Moritz, J. Zaanen, T. P. Devereaux, W. S. Lee, Electronic structure of the parent compound of superconducting infinite-layer nickelates. *Nat. Mater.* **19**, 381–385 (2020).

46. M. J. Sayagués, M. Vallet-Regí, A. Caneiro, J. González-Calbet, Microstructural characterization of the LaNiO₃₋y system. *J. Solid State Chem.* **110**, 295–304 (1994).

47. R. D. Sánchez, M. T. Causa, A. Caneiro, A. Butera, M. Vallet-Regí, M. J. Sayagués, J. González-Calbet, F. García-Sanz, J. Rivas, Metal-insulator transition in oxygen-deficient LaNiO₃₋x perovskites. *Phys. Rev. B* **54**, 16574–16578 (1996).

48. E. Benckiser, M. W. Haverkort, S. Brück, E. Goering, S. Macke, A. Frañó, X. Yang, O. K. Andersen, G. Cristiani, H.-U. Habermeier, A. V. Boris, I. Zegkinoglou, P. Wochner, H.-J. Kim, V. Hinkov, B. Keimer, Orbital reflectometry of oxide heterostructures. *Nat. Mater.* **10**, 189–193 (2011).

49. M. Wu, E. Benckiser, M. W. Haverkort, A. Frano, Y. Lu, U. Nwankwo, S. Brück, P. Audehm, E. Goering, S. Macke, V. Hinkov, P. Wochner, G. Christiani, S. Heinze, G. Logvenov, H.-U. Habermeier, B. Keimer, Strain and composition dependence of orbital polarization in nickel oxide superlattices. *Phys. Rev. B* **88**, 125124 (2013).

50. A. S. Disa, F. Walker, S. Ismail-Beigi, C. H. Ahn, Research update: Orbital polarization in LaNiO₃-based heterostructures. *APL Mater.* **3**, 062303 (2015).

51. J. Zhang, A. S. Botana, J. W. Freeland, D. Phelan, H. Zheng, V. Pardo, M. R. Norman, J. F. Mitchell, Large orbital polarization in a metallic square-planar nickelate. *Nat. Phys.* **13**, 864–869 (2017).

52. Z. Liao, E. Skoropata, J. W. Freeland, E.-J. Guo, R. Desautels, X. Gao, C. Sohn, A. Rastogi, T. Z. Ward, T. Zou, T. Charlton, M. R. Fitzsimmons, H. N. Lee, Large orbital polarization in nickelate-cuprate heterostructures by dimensional control of oxygen coordination. *Nat. Commun.* **10**, 589 (2019).

53. K. Thompson, D. Lawrencea, D. J. Larsona, J. D. Olsona, T. F. Kellya, B. Gormanb, In situ site-specific specimen preparation for atom probe tomography. *Ultramicroscopy* **107**, 131–139 (2007).

54. A. Jain, S. P. Ong, G. Hautier, W. Chen, W. D. Richards, S. Dacek, S. Cholia, D. Gunter, D. Skinner, G. Ceder, K. A. Persson, Commentary: The materials project: A materials genome approach to accelerating materials innovation. *APL Mater.* **1**, 011002 (2013).

55. G. Kresse, J. Furthmüller, Efficient iterative schemes for *ab initio* total-energy calculations using a plane-wave basis set. *Phys. Rev. B* **54**, 11169–11186 (1996).

56. G. Kresse, D. Joubert, From ultrasoft pseudopotentials to the projector augmented-wave method. *Phys. Rev. B* **59**, 1758–1775 (1999).

57. J. P. Perdew, A. Ruzsinszky, G. I. Csonka, O. A. Vydrov, G. E. Scuseria, L. A. Constantin, X. Zhou, K. Burke, Restoring the density-gradient expansion for exchange in solids and surfaces. *Phys. Rev. Lett.* **100**, 136406 (2008).

58. A. I. Liechtenstein, V. I. Anisimov, J. Zaanen, Density-functional theory and strong interactions: Orbital ordering in Mott-Hubbard insulators. *Phys. Rev. B* **52**, R5467–R5470 (1995).